Analysis of Poly(ethylene terephthalate) (PET) Films by Atomic Force Microscopy

S. A. C. GOULD,[1] D. A. SCHIRALDI,[2] M. L. OCCELLI[3]

[1] Keck Science Center, Claremont Colleges, Claremont, California 91711

[2] Hoechst Celanese, Corp., P.O. Box 32414, Charlotte, North Carolina 28232

[3] GTRI, Georgia Institute of Technology, Atlanta, Georgia 30332

Received 12 September 1996; accepted 1 November 1996

ABSTRACT: An atomic force microscope operating in a contact mode can provide 5- × 5-nm atomic-scale images of a poly(ethylene terephthalate) (PET) film that allows the identification of what are believed to be phenyl groups and phenyl chains. Large-scale, 5- × 5-μm images reveal the presence of raised surface features attributed to the extrusion process used to form the PET film. These surface irregularities could affect the film's physicochemical properties. Furthermore, regions with different overall surface roughnesses have been identified, showing that surface roughness can distinguish between the amorphous and crystalline regions that form this type of film. Imaging forces have been found capable of altering the film surface, and surface disorder increases with imaging time. © 1997 John Wiley & Sons, Inc. J Appl Polym Sci **65:** 1237–1243, 1997

Key words: atomic force microscope; surface roughness; poly(ethylene terephthalate) film; crystalline regions; amorphous regions

INTRODUCTION

Since Binnig and coworkers[1] invented the atomic force microscope (AFM), this type of scanning probe microscopy has been proven particularly useful in providing details of nonconducting surfaces at the atomic-scale level. It is now possible to image polymers,[2–8] biological materials,[9–12] clays,[13–15] metal sulfides,[16] glasses,[17] metal oxides,[18] zeolites,[19–22] and zeolite-containing catalysts used by petroleum engineers to produce transportation fluids.[23,24] It is the purpose of this article to report the use of AFM to investigate the surface of poly(ethylene terephthalate) (PET) films.

EXPERIMENTAL

A 1- × 1-cm sample of commercial grade HOSTOPHAN® PET film, obtained by melt extrusion of a PET polymer, was used as sample PET-F in this study. This polymer was produced by reacting ethylene glycol and terephthalic acid using an Sb_2O_3 catalyst. Samples PET-W and PET-SH are similar films obtained from the front wall and shoulder of a commercially produced, terephthalic acid-modified PET soft-drink bottle. These films were glued onto steel disks with epoxy resin. After the glue dried, the AFM tip was carefully guided to the middle of the film, thus beginning the imaging session.

The AFM used for these experiments[25] was a contact-mode instrument (Nanoscope III; Digital Instruments, Santa Barbara, CA) based on the optical lever cantilever detection design of Meyer and Amer[26] and Alexander and colleagues.[27] The images presented in this paper contain either 256 × 256 or 512 × 512 data points, and nearly all the images shown in the figures were acquired within a few seconds. The Si_3N_4 cantilevers (with integral tips) used for imaging were between 60

Correspondence to: M. L. Occelli.

 CCC 0021-8995/97/071237-07

and 120 μm in length and possessed a spring constant in the 0.1–0.6-N/m range. In general, the force applied for these images ranged from 1.0 to 100 nN. Several hundred images were examined using different cantilevers. As before, the AFM was calibrated by imaging mica.

The mean surface roughness (R_a) of several AFM images was studied by examining variations in the average vertical range (z-values) exhibited by the image and is defined by

$$R_a = \frac{1}{L_x L_y} \int_0^{L_x} \int_0^{L_y} |f(x, y)| \, d_x d_y$$

where $f(x, y)$ is the surface relative to the image center plane, and L_x and L_y are the dimensions of the surface.[28] The largest vertical-range variation measured in an image is expressed by R_m, which is the distance between the highest and lowest points on the surface relative to the mean plane.[28]

RESULTS AND DISCUSSION

In an AFM, an *xyz* piezoelectric translator raster scans a sample below the stylus of the cantilever. The vertical deflection (z-direction) of the cantilever is measured as the stylus moves over the topography of the surface, by reflecting a laser beam off the end of the cantilever and measuring the location of the reflected laser light with a two-segment photodiode.[8] A digital electronic feedback loop keeps the deflection of the cantilever, and therefore the force of the stylus on the surface, constant. This is accomplished by moving the sample up and down in the z-direction of the *xyz* translator as the sample is scanned in the x- and y-directions.[8]

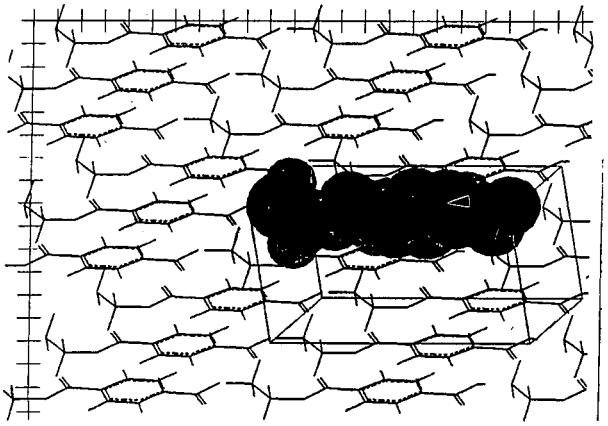

Figure 1 Schematic representation of the PET structure.

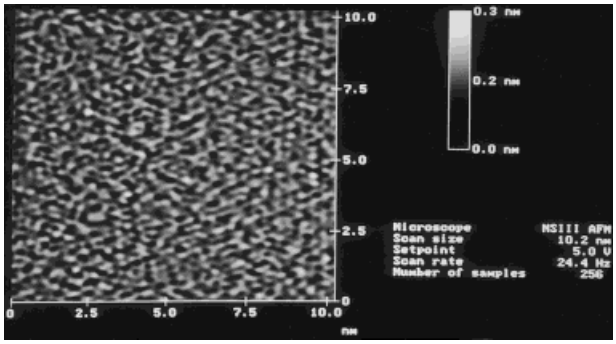

Figure 2 Top view, atomic-scale image of sample PET-SH.

The atomic-scale images in Figures 2–6 provide structural details that cannot be totally correlated to the schematic representation of the PET structure shown in Figure 1. However in Figures 2–6 and in other images (not shown), it is possible to observe sets of three white spots, 0.29 nm in diameter, generating short chains 0.7 nm (±0.1 nm) in length (Fig. 5). These white spots are believed to represent phenyl rings in the PET structure. If we let the C—C bond length in benzene be 0.14 nm, then a benzene ring will offer the AFM tip a target area at least 0.28 nm in diameter. Using the scale in Figure 1, a length of about 0.94 nm can be obtained for the three-phenyl-rings chain.

Figures 2–6 show the absence of the preferential orientation of the alkyl chains connecting phenyl groups as shown in Figure 1. The lack of periodicity in these atomic-scale images could be attributed to the extrusion process or, more likely, to a lack of complete structural rigidity in the different PET films that allows the occurrence of surface deformation by the AFM imaging forces.

In fact, although the applied force was in the

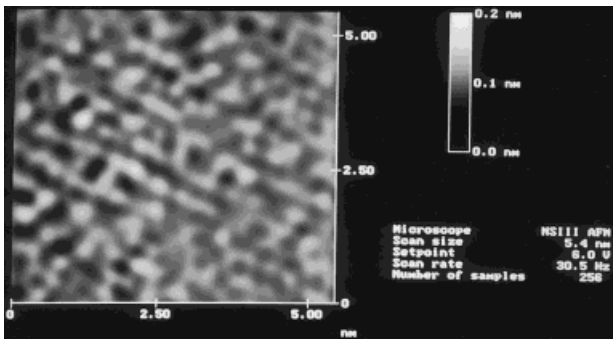

Figure 3 Top view, atomic-scale image of sample PET-W.

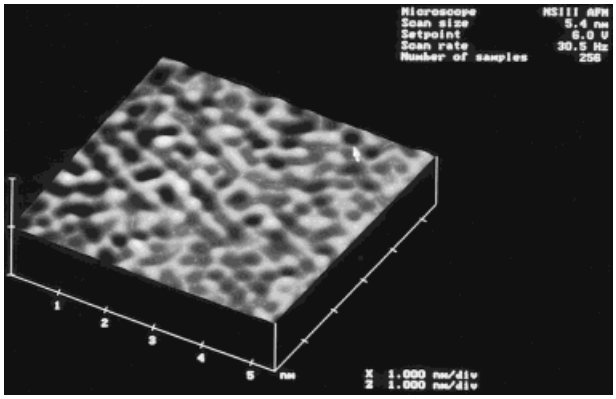

Figure 4 Side view of Figure 3.

1.0–100-nN range, the tip of the cantilever was found capable of modifying the PET surface topography. In an effort to measure surface deformation as a function of force and time, a silicon tip with an imaging force of 100 nN was used to generate the results reported in Figure 7. It can be observed that in Figure 7, after raster scanning of a 1- × 1-μm region of the film for about 46 s, a permanent indentation was generated on the surface, and that the surface topography changed with time [Fig. 7(b–d)]. Specifically, after scanning for 4 s, the mean roughness (R_a) and maximum height (R_m) of the surface shown in Figure 7(b) were 2.4 and 24.2 nm, respectively. Images were then collected at 2-s intervals for a 46-s period. R_a and R_m values monotonically increased to 5.7 nm and 49.4 nm, respectively. Figure 7(d) shows a large (10- × 10-μm) image containing a 1- × 1-μm area indicating the results of the deformation experiment.

Similar results were obtained after imaging other sections of the same 10- × 10-μm region and

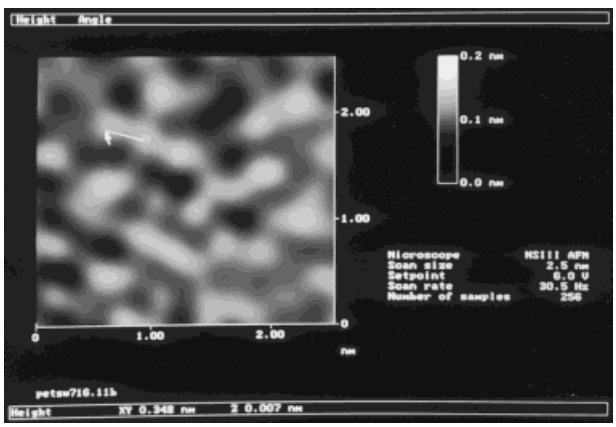

Figure 5 Top view, atomic-scale image of sample PET-W showing possible chains of phenyl rings.

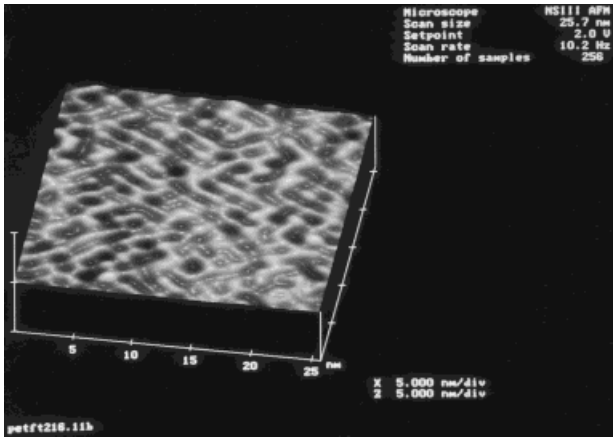

Figure 6 Side view, atomic-scale image of sample PET-F; contains some details also seen in Figure 5.

after imaging PET-SH and PET-F samples [Fig. 7(e,f)]. Thus, for imaging forces in the range of 1.0–100 nN, the AFM tip was found capable of altering the surface of these PET samples [Fig. 7(a–d)].

The large (10- × 10-μm) images in Figures 7–13 reveal the existence of raised surface features that form almost parallel ridges aligned along (what is believed to be) the film extrusion direction. Cross-sectional analysis of these surfaces indicates that the ridges are an average of 1.0 μm ($\pm$0.2 μm) wide and that the average spacing between ridges is near 1.2 μm ($\pm$0.1 μm). Similarly, in Figures 9 and 10, overall surface roughness profiles give R_a and R_m values of 3.6 and 42.0 nm, respectively. In Figures 7(f) and 8 the collection of parallel ridges is crossed at a 60-degree angle by a ridge 3–4 nm in height. The patterns in Figures 7–13 could indicate possible reorientation of the PET chains during the extrusion process. Surface modifications of the type shown in Figures 7–13 could affect the extruded PET films' physicochemical and mechanical properties.

The schematic representation of the PET film macrolattice[29] in Figure 12 proposes that the PET structure is formed by a regular distribution of oriented microfibril (chains) aggregates aligned along the fiber axis.[29] These regions of crystallinity are held together by tie microfibrils oriented in a fairly random manner, thus forming amorphous domains regularly dispersed between the crystalline regions (Fig. 12).

The large-scale images in Figure 13(a,b) contrast two 5- × 5-μm sections of the PET film in which surface chains are well oriented side by side [as in Fig. 13(a)] or have variable length and orientation [as in Fig. 13(b)]. It is believed that

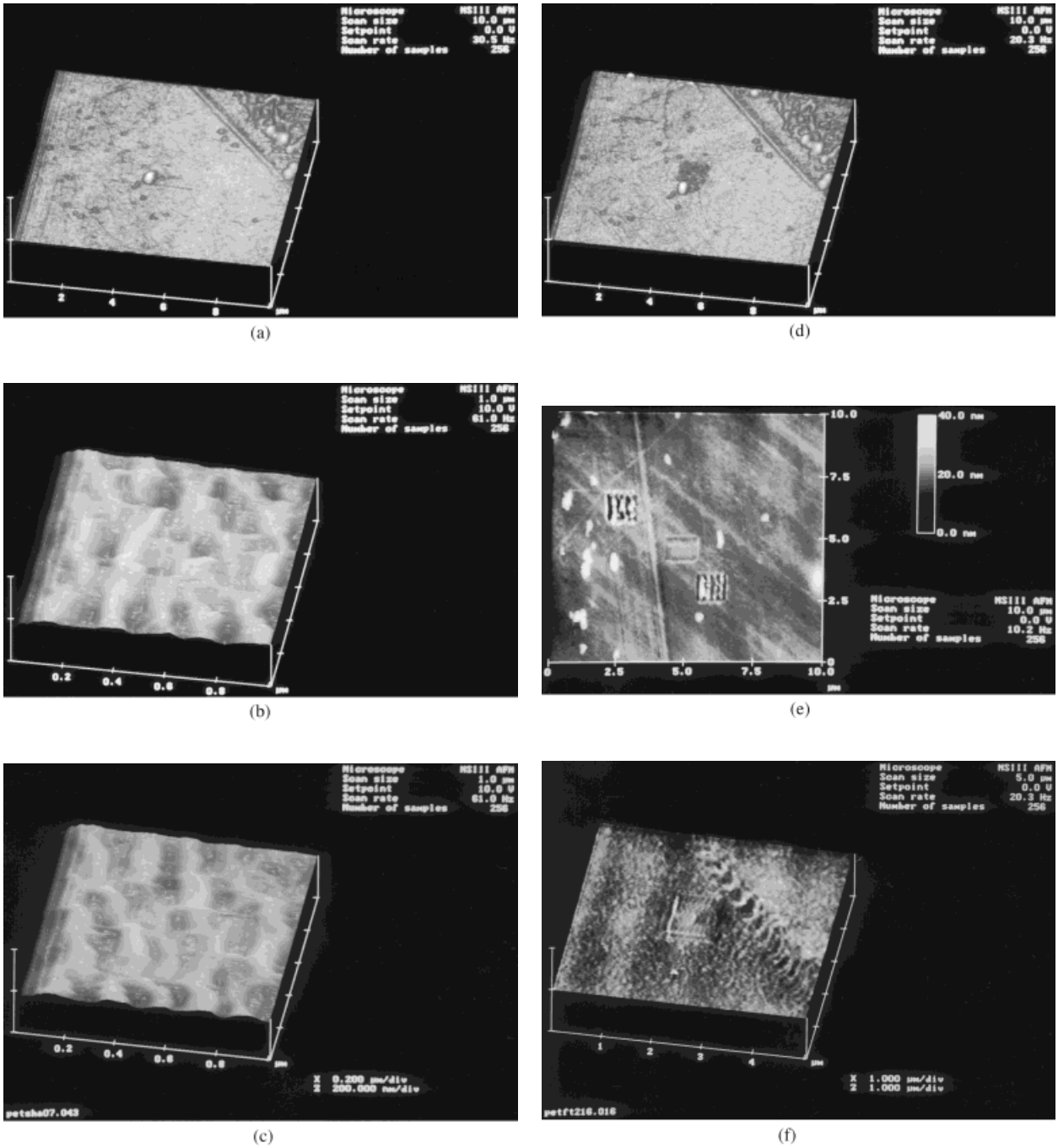

Figure 7 (a) Side view, large-scale image of sample PET-SH at the beginning of the imaging session. (b) Side view, large-scale image showing surface modification in sample PET-SH after 4 s. (c) Side view, large-scale image showing surface modifications in sample PET-SH after 8 s. (d) Side view of large-scale image in (a) at the end of the imaging session. White arrow points to a 1- $\times$ 1-μm area modified by the imaging force. (e) Top view, large-scale image of sample PET-SH showing three 1- $\times$ 1-μm zones modified by the imaging force. (f) Top view, large-scale image of sample PET-F showing surface modification by the imaging force.

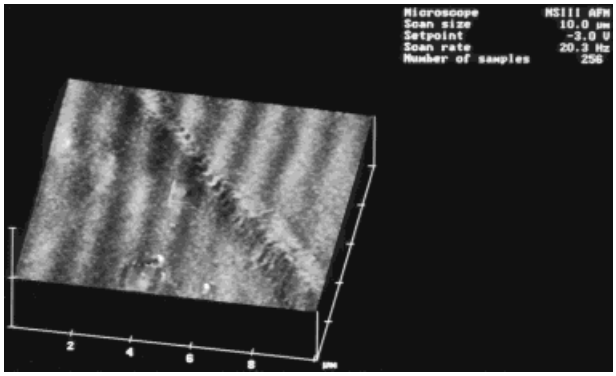

Figure 8 Side view, large-scale image of sample PET-F showing raised surface features typical of this type of materials. The film was prepared by melt extrusion of a PET polymer. The image contains two 1.0- × 1.0-μm indentations resulting from surface modification by the imaging force.

these two regions represent crystalline and amorphous domains, respectively. In Figure 13(a), a 2- × 2-μm section on the right-hand side has R_a of 2.3 nm and R_m of 19.3 nm. In contrast, a similar section in Figure 13(b) was found to have R_a of 24 nm and R_m of 191 nm. Areas with R_a and R_m values of 37.7 and 314 nm, respectively, were observed in other parts of Figure 13(b). These measurements indicate that a large difference in surface roughness exists between the crystalline and amorphous regions.

These two types of aggregates can also be observed in the same 10- × 10-μm large-scale image in Figure 13(c). The white arrows in Figure 13(d) (bottom) indicate the boundary between the amorphous and crystalline domains. A second arrow points to tie microfibrils[29] that separate these two regions and then extend into the neighboring domains [Fig. 13(d)]. As expected from the images in Figure 13(a,b), the two domains

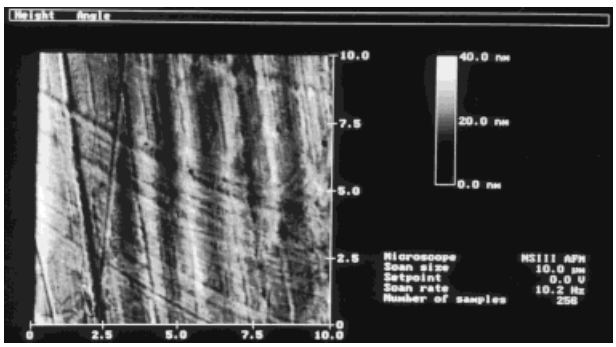

Figure 9 Top view, large-scale image of sample PET-W from the front part of a bottle, showing the same type of surface features seen in sample PET-F.

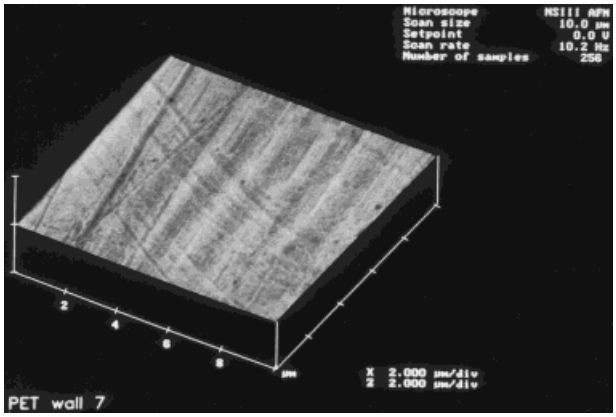

Figure 10 Side view of Figure 9.

have distinguishing roughness properties. In Figure 13(b), the crystalline region has R_a of 13.2 nm and R_m of 120 nm. In the adjacent amorphous region these values increases to 22.8 and 154 nm, respectively.

It should be kept in mind that the AFM probably underestimates the height of the surface roughness measured because the AFM tip is pyramidal with sides at 45 degrees, and has a radius of curvature estimated at 20–40 nm.[30] As a result, it may not be able to faithfully trace and describe the steep and sometime deep grooves found on these types of surfaces. Nevertheless, in contrast to the representation shown in Figure 12, AFM images in Figure 13(a–d) indicate that crystalline and amorphous microfibril domains in PET fibers are fairly irregular in size and shape, they have different and distinguishable surface roughnesses, and their distribution does not follow any preestablished pattern.

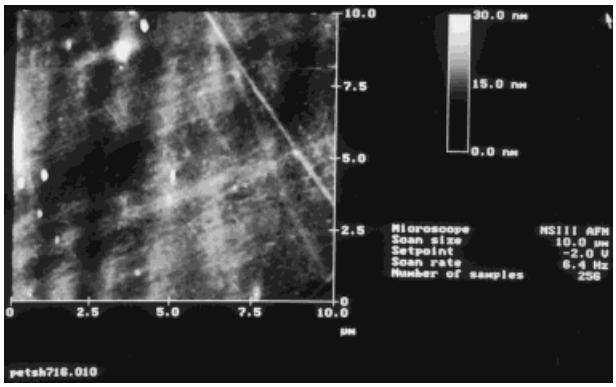

Figure 11 Top view, large-scale image of sample PET-SH from the shoulder of a bottle, showing the same type of surface features seen in samples PET-F and PET-W.

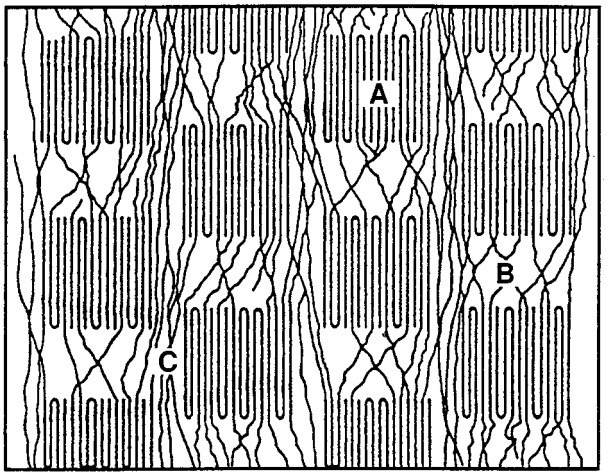

Figure 12 Schematic representation of the PET film macrolattice (30). A and B represent crystalline and amorphous regions connected by the tie microfibrils indicated in C.

SUMMARY AND CONCLUSIONS

When an AFM is operated in a contact mode, the tip of the cantilever is in constant contact with the sample surface, where it fluctuates according to the surface topography in a manner controlled by repulsive van der Waals's forces. This mode of operation provides high resolution and the possible identification of phenyl groups and phenyl chains as shown in Figures 2–6, but it can also provide artifacts resulting from morphologic deformation induced by the rigidity of the cantilever in contact with the surface (Fig. 7).

Rough surfaces cannot generally be traced accurately because of the finite radius of curvature of the tip. Thus the surface topography of the PET samples under study has been traced with an accuracy controlled by the tip size and by the cantilever spring constant. Furthermore, the interpre-

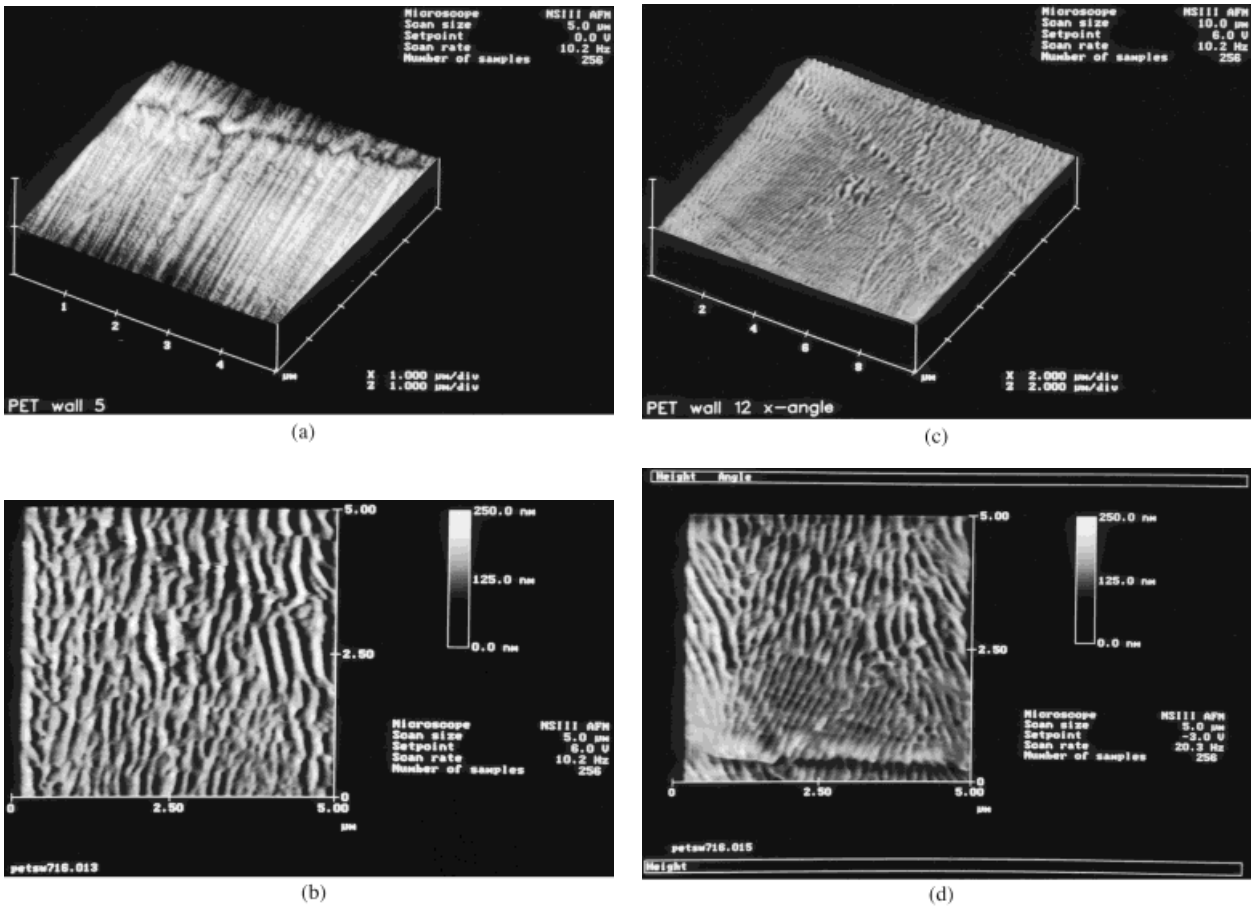

(a) (c) (b) (d)

Figure 13 (a) Side view, large-scale image of sample PET-W showing a possible crystalline zone of the film. (b) Top view, large-scale image of sample PET-W showing a possible amorphous zone in the film. (c) Side view, large-scale AFM image of sample PET-W. Arrows indicate possible amorphous and crystalline zones. (d) Top view, large-scale image of sample PET-W showing the boundary (arrow) between amorphous and crystalline domains.

tation of images in Figures 7–13 was assisted by taking side views and by rotating the images in different directions.

By rotating the image, changing scan speeds and time, and changing the imaging force, artifacts can be separated from real features. In this way, it is possible to observe surface deformations that could affect the physicochemical properties of commercially available PET bottles and also possible to use roughness measurements to locate crystalline and amorphous regions in PET films.

The assistance in obtaining Figure 1 and the useful discussions with L. Arney of the Hoechst Celanese Company are gratefully acknowledged.

REFERENCES

1. G. Binnig, H. Rohrer, C. Gerber, and E. Weibel, *Phys. Rev. Lett.,* **50,** 120 (1983).
2. R. Patil, S. J. Kim, E. Smith, D. H. Reneker, and A. L. Weisenhorn, *Polym. Commun.,* **31,** 455 (1990).
3. S. N. Magonov, K. Qvarnstrom, V. Elings, and H. J. Cantow, *Polym. Bull.,* **25,** 689 (1991).
4. B. Lotz, J. C. Wittmann, W. Stocker, S. N. Magonov, and H. J. Cantow, *Polym. Bull.,* **26,** 209 (1991).
5. P. C. M. Grim, H. J. Brouwar, R. M. Seyger, G. T. Oostergetel, W. G. Bargama-Schutter, A. C. Arnberg, P. Guthner, K. Dransfeld, and G. Hadziioannou, *Makromol. Chem., Macromol. Symp.,* **62,** 141 (1992).
6. S. N. Magnov and H. J. Cantow, *J. Appl. Polym. Sci.: Appl. Polym. Symp.,* **90,** 7550 (1989).
7. D. W. Schwark, D. L. Vezie, J. R. Reffner, and E. L. Thomas, *J. Mater. Sci. Lett.,* **11,** 352 (1992).
8. S. A. C. Gould, B. Drake, C. D. Prater, A. L. Weisenhorn, S. M. Lindsay, and P. K. Hansma, *Proc. 47th Ann. Meet. Electron Microsc. Soc. Am.,* G. W. Bailey, ed., 1989.
9. E. Henderson, *J. Microsc.,* **167,** 77 (1992).
10. V. S. Kulkarni, W. H. Anderson, and R. E. Brown, *USA Microsc. Analysis,* **January,** 13 (1995).
11. S. A. C. Gould, et al., *J. Vac. Sci. Technol.,* **A8**(1), (1990).
12. B. Drake, C. B. Prater, A. L. Weisenhorn, S. A. C. Gould, T. R. Albrecht, C. F. Quate, D. S. Cannell, H. G. Hansma, and P. K. Hansma, *Science,* **243,** (1990).
13. H. Hartman, G. Sposito, A. Yang, S. Manne, S. A. C. Gould, and P. K. Hartman, *Clays Clay Miner.,* **38**(4), 337 (1990).
14. M. L. Occelli, B. Drake, and S. A. C. Gould, *J. Catal.,* **142,** 337 (1993).
15. M. L. Occelli, B. Drake, and S. A. C. Gould, *Microporous Mater.,* **2,** 205 (1994).
16. S. Foglia, A. G. Tomlinson, S. Mulley, and A. Sironi, *J. Mater. Chem.,* **5,** 1191 (1995).
17. D. M. Kujorwansa, L. C. Jensen, S. C. Langford, and J. T. Dickinson, *J. Mater. Res.,* **9,** 476 (1994).
18. Y. Carmi, A. J. Dahm, S. J. Eppell, W. Jennings, R. E. Marchant, and G. M. Michael, *J. Vac. Technol.,* **B10,** 2302 (1992).
19. M. Komiyama and T. Yashima, *Jpn. J. Appl. Phys.,* **22,** 3761 (1994).
20. A. L. Weisenhorn, J. E. MacDougall, S. A. C. Gould, S. D. Cox, W. S. Wise, J. Massie, P. Maivald, V. B. Elings, G. D. Stucky, and P. K. Hansma, *Science,* **247,** 1330 (1990).
21. J. E. MacDougall, S. D. Cox, G. D. Stucky, A. L. Weisenhorn, P. K. Hansma, and W. S. Wise, *Zeolites,* **June,** 11 (1991).
22. L. Scandella, N. Kruse, and R. Prins, *Surface Sci. Lett.,* **281,** L331 (1993).
23. M. L. Occelli and S. A. C. Gould, *CHEMTECH,* **May,** 24 (1994).
24. M. L. Occelli and S. A. C. Gould, in *ACS Symposium Series,* Vol. 571, M. L. Occelli and P. O'Connor, eds., ACS, Washington, DC, p. 271 (1994).
25. G. Binnings, C. F. Quate, and C. Gerbr, *Phys. Rev. Lett.,* **56,** 430 (1986).
26. G. Meyer and N. M. Amer, *Appl. Phys. Lett.,* **53,** 1095 (1988).
27. S. Alexander et. al., *J. Appl. Phys.,* **65,** 164 (1989).
28. NanoScope III, Version 3.0, Command Reference Manual, December 1993.
29. D. C. Prevorsek, G. A. Tirpak, P. J. Harget, and A. C. Reimschuessel, *J. Polym. Sci., Polym. Phys. Ed.,* **B9**(4), 733 (1974).
30. S. Akamine, R. C. Barrett, and C. F. Quate, *Appl. Phys. Lett.,* **57,** 316 (1990).